

Simulation of Near-Fault Strong-Ground Motion Using Hybrid Green's Functions

by Arben Pitarka, Paul Somerville, Yoshimitsu Fukushima, Tomiichi Uetake,
and Kojiro Irikura

Abstract The recently proposed hybrid Green's function method is designed to combine the advantages of both deterministic and stochastic approaches to simulating broadband ground motion when records of small events are not available. The method has the flexibility of incorporating complexities in the source, wave path, and local-site effects into strong ground motion simulations. In this article we analyze its effectiveness at simulating near-fault ground motions by comparisons with the empirical source time function method, empirical ground-motion-attenuation relations, and recorded near-fault ground motion. We present a simple model for introducing the effect of the radiation pattern to the stochastic Green's functions in the intermediate frequency range (1–3 Hz). The numerical test results of the method and the generally good agreement between simulated and recorded ground motion from the 17 January 1995 Kobe earthquake shown in this study indicate that the technique has the capability of reproducing the main characteristics of near-fault ground motion.

Introduction

The challenge of near-fault broadband simulation techniques is to provide ground motions with characteristics that match recorded ground motions affected by various source process and underground structure conditions. Recent analyses of ground motions from damaging earthquakes show that near-fault ground motions are characterized by long-period pulses caused by the forward rupture directivity of the source and amplified as the waves propagate into adjacent basins, which are often fault controlled. The period, duration, and amplitude of such pulses has a significant impact on the response of buildings during strong earthquakes. Most of the long-period characteristics of near-fault motions can be well simulated using deterministic methods based on kinematic slip models and heterogeneous crustal models. On the other hand, stochastic models (e.g., Hanks and McGuire 1981; Joyner and Boore, 1986; Silva *et al.*, 1995; Beresnev and Atkinson, 1998) do not provide a good representation of near-fault ground motions in time domain, but they perform well at predicting the amplitude and frequency content of motion, on average, at long distances and over a wide frequency range. Chin and Aki (1991) extended the random-vibration technique to include the effects of the finite-fault rupture and site-amplification factors. However, phase effects due to the propagation path and site response are not included in their approach.

Hybrid techniques that combine both deterministic and empirical approaches can increase the effectiveness of

broadband strong ground motion simulation if recordings of small earthquakes are not available (e.g., Hartzell *et al.*, 1999). The empirical source time function (ESF) technique proposed by Hadley *et al.* (1982) is one of them. Their method was later improved by Wald *et al.* (1988) and Somerville *et al.* (1991) by introducing an empirical representation of the radiation pattern using empirical source functions. The summation of the Green's functions is done using Hartzell's technique (1978). The method proved to be very effective for simulating ground motions from large earthquakes (e.g., Cohee *et al.*, 1991; Somerville, 1993; Graves *et al.*, 1996).

Recently Kamae *et al.* (1998) proposed a new hybrid technique for simulating near-fault ground motion, which combines deterministic and stochastic approaches to generate synthetic Green's functions and uses composite-source modeling. The stochastic approach used to simulate the high-frequency part of the Green's function is based on the Brune omega-squared point-source model. The strong-ground motion from a finite fault is then calculated by summing up the synthetic Green's functions representing the response of subfaults using Irikura and Kamae's (1994) summation technique. As demonstrated by Atkinson and Silva (1997), this finite-fault model correctly matches the observed spectral shapes and amplitude. The technique of Kamae *et al.* (1998) was successfully applied to simulating ground motions from the Kobe, Japan, earthquake. How-

ever, their representation of the radiation pattern effect was limited to the low-frequency range. In this article we introduce a simple technique that extends the effect of the radiation pattern to the intermediate-frequency range (1–3 Hz). We analyze the effectiveness of the hybrid Green's function technique at simulating near-fault ground motions by comparisons with the ESF method, empirical ground-motion-attenuation relations, and recorded near-fault ground motion.

Methodology

The hybrid Green's function (HGF) method is an extension of the semiempirical Green's function method. It has been described in detail by Kamae *et al.* (1998). Here we outline some important aspects and improvements of the technique for generating hybrid Green's functions. The HGF method is based on the composite-source-modeling technique. The mainshock fault plane is divided into subfaults, each of them representing the rupture area of a small event. The number of subfaults N is determined from equation (1) assuming that the mainshock and the small event have the same stress drop:

$$N = (M_{0m}/M_{0s})^{2/3} \quad (1)$$

where M_{0m} and M_{0s} are the seismic moments for the mainshock and the small event, respectively.

The mainshock seismogram $U(\mathbf{X}, t)$ at a vector position \mathbf{X} is calculated by summing up the synthetic seismograms $u(\mathbf{X}, t)$ representing the response of each subfault as follows (Irikura and Kamae, 1994):

$$U(\mathbf{X}, t) = \sum_{i=1}^N C_i \frac{r}{r_i} F(t - t_i) * u(\mathbf{X}, t) \quad (2)$$

where:

$$C_i = \Delta\sigma_i/\Delta\sigma_s$$

$$t_i = (r_i - r_o)/\beta + \xi_i/V_r$$

$$F(t) = \delta(t) + \frac{1}{n} \sum_{k=1}^{(N-1)n} \delta \left[t - (k - 1) \frac{\tau}{(N - 1)n} \right]$$

C_i is the ratio of the stress drop $\Delta\sigma_i$ in the subfault i and that of the small event $\Delta\sigma_s$, r , r_i , and r_o are the distances from the site to the hypocenter of the small event, from the site to i th subfault, and from the site to the starting point of rupture on the fault, respectively. ξ_i is the distance between the starting point and the i th subfault. β , V_r , and τ are shear-wave velocity, rupture velocity, and the rise time of the large event, respectively. n is an arbitrary integer number used to shift the artificial periodicity to a frequency higher than that of interest. A stochastic component is included in the speed of the rupture propagation to simulate the heterogeneities in the kinematics of the rupture.

Kamae *et al.* (1998) tested the technique using fault models with the stress-drop ratio fixed at a constant value within the asperities and zero elsewhere on the fault. Here we consider a more general case where large scale asperities are introduced by varying the stress drop over the fault surface. The stress drop ratio C_i that appears in equation (2) is calculated using the approach proposed by Frankel (1995). Frankel's technique satisfies the condition that the high-frequency spectral level of the Green's function sum should equal that of the mainshock. Also the root mean square stress drop over the mainshock fault plane should be equal to the stress drop of the small event $\Delta\sigma_s$:

$$\left(\frac{\sum_{i=1}^N \Delta\sigma_i^2 A_s}{A_m} \right)^{1/2} = \Delta\sigma_s \quad (3)$$

where A_s and A_m are the areas of the subfault and main event, respectively.

Often the source model for a scenario earthquake is represented by the final slip distribution on the fault. To derive the stress drop-ratio distribution C_i from the slip distribution d_i on the fault we assume that they are proportional:

$$C_i = \alpha d_i/d_{\max} \quad (4)$$

where d_{\max} is the maximum slip; α can be determined by substituting equation (4) into equation (3) and rearranging:

$$\alpha = \left(\frac{\frac{A_m}{A_s}}{\sum_{i=1}^N \left(\frac{d_i}{d_{\max}} \right)^2} \right)^{1/2} \quad (5)$$

The procedure we used to calculate hybrid Green's functions is similar to the original one in that it computes the low- and high-frequency ranges separately and then combines the two of them to produce a single time history. The low-frequency part of the HGF is generated deterministically using numerical techniques that take into consideration the wave propagation and site effects. The high-frequency part is calculated by a stochastic approach using random vibration time series with a Brune (1970) far-source spectrum and a frequency-dependent radiation-pattern model.

Radiation-Pattern Model

While at low frequencies the radiation pattern of waves radiated from the seismic source is readily observed; at high frequencies the pattern is not as clear. Based on analysis of peak accelerations from the Whittier Narrows, California, earthquake and an aftershock, Vidale (1989) argued that for this earthquake the standard double-couple radiation pattern

is observable in the frequency range of 3–6 Hz. On the other hand, analysis of the ground motion from the 1979 Imperial Valley earthquake and an aftershock (Liu and Helmberger, 1985) show a double-couple pattern at frequencies smaller than 1 Hz but not at 2 Hz or higher. The frequency-dependence of the radiation pattern is probably due to scattering from small-scale heterogeneities in the fault zone and around the recording station that tend to affect a broad range of frequencies. The distribution of these heterogeneities is assumed to be random, and the degree of randomness is assumed to increase with frequency.

In order to account for the frequency-dependent radiation-pattern effect, we have used average radiation coefficients that produce a gradual decay of the radiation pattern effect as a function of frequency (Kamae and Irikura, 1992). We incorporated the frequency-dependent radiation pattern into the computation of the HGF. In the tests shown in this article the radiation pattern at frequencies lower than 1 Hz is modeled using theoretical radiation coefficients of body waves for a double-couple point source. At the intermediate frequency range 1–3 Hz we used average radiation coefficients for body waves. They are calculated using the technique proposed by Boore and Boatwright (1984) assuming a variable range of takeoff angles that is modeled as a linear function of frequency. This approach works under the assumption that the waves that carry the energy contributing to the peak acceleration are body waves coming directly from the source and have takeoff and azimuth angles randomly distributed within given ranges. At frequencies higher than 3 Hz we used a constant average radiation coefficient calculated at that frequency. Figure 1 illustrates the frequency-dependent radiation pattern of *SH* waves for a point source with pure strike-slip mechanism calculated with the proposed approach.

The choice of the frequency limits 1 Hz and 3 Hz used in this study is based on the fact that the deterministic approach to modeling underground structure and the source process is usually reliable at low frequencies only (less than 1 Hz), and on the frequency dependence of the coherence of the radiation pattern analyzed by Liu and Helmberger (1985). In the following section we describe the technique we used to calculate average body-wave radiation coefficients.

Average Body-Wave Radiation Coefficients

Most broadband simulations that apply random vibration theory use the *S*-wave rms average radiation coefficient. This average is independent of the fault orientation and in general is calculated over the whole focal sphere, which makes the near-fault ground-motion modeling inaccurate at low frequencies. In our application only a portion of the focal sphere is sampled using a range of appropriately chosen takeoff angles. The radiation coefficients of *SV* and *SH* waves are averaged over a range of azimuth and takeoff

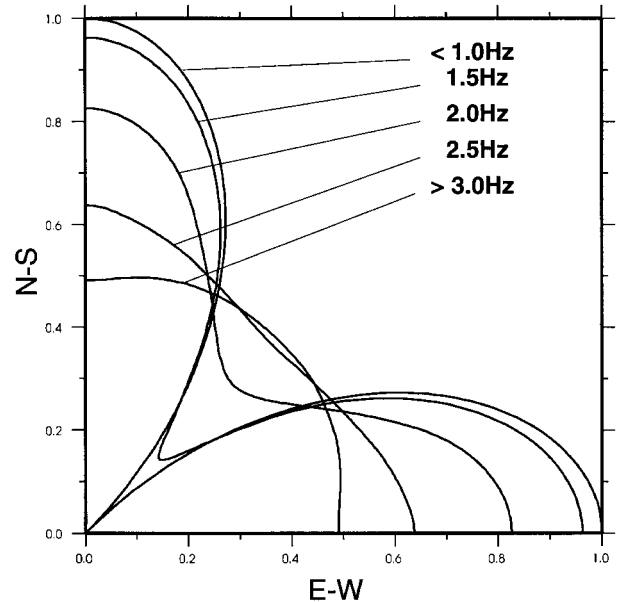


Figure 1. Frequency-dependent *SH*-wave radiation pattern for a point source with a pure strike-slip mechanism and an azimuth angle of 0 degrees. Note that at frequencies higher than 3 Hz the radiation effect is assumed as purely stochastic; therefore, the radiation pattern transforms into a circle.

angles randomly distributed using Boore and Boatwright's technique (1984).

Following their technique the radiation coefficient for a given type of wave can be calculated using the expression

$$\langle G \rangle = \frac{\int_0^\pi \int_0^{2\pi} [W(\theta, \phi)G(\theta, \phi)] \sin(\theta) d\phi d\theta}{\int_0^\pi \int_0^{2\pi} [W(\theta, \phi)] \sin(\theta) d\phi d\theta} \quad (6)$$

where ϕ is the azimuth and θ is the takeoff angle. It is assumed that the weighting function $W(\theta, \phi)$ is nonzero and equal to one for takeoff angles θ in the range $\theta_1 < \theta < \theta_2$ and azimuth angles ϕ in the range of $(\phi_r - \phi_1) < \phi < (\phi_r + \phi_1)$ where ϕ_r is the receiver azimuth.

The integral in equation (10) is evaluated using a Monte Carlo scheme (Boore and Boatwright, 1984). According to that scheme the average value of the radiation coefficient G can be evaluated as the average coefficient evaluated at M pairs of θ_i and ϕ_i

$$\langle G \rangle = \frac{1}{M} \sum_{i=1}^M G(\theta_i, \phi_i) \quad (7)$$

where θ_i, ϕ_i are calculated based on M random numbers η_i, χ_i between 0 and 1 that are mapped as follows:

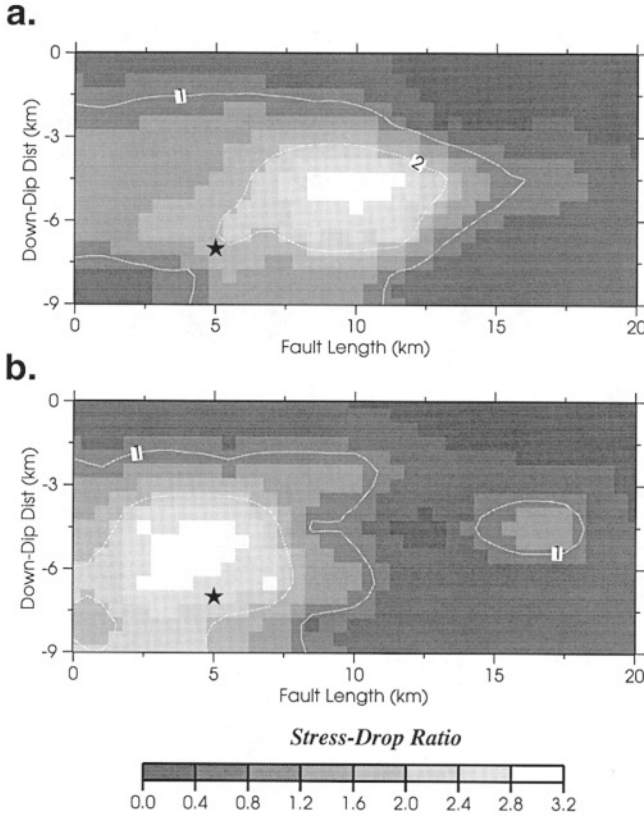


Figure 2. Two different stress-drop-ratio models used to simulate broadband time histories of the ground motion from a M 6.5 earthquake using synthetic Green's functions from a M 4.6 small event.

$$\begin{aligned}\theta_i &= \cos^{-1} [(1 - \xi_i) \cos \theta_1 + \xi_i \cos \theta_2] \\ \phi_i &= \phi_r + \phi_1(0.5 - \eta_i).\end{aligned}\quad (8)$$

The frequency dependence of the radiation coefficients is introduced by expressing θ_1 , θ_2 , and ϕ_1 as linear functions of frequency between f_1 and f_2 :

$$\begin{aligned}\theta_1 &= \theta_r - \pi/6 (f - f_1)/(f_2 - f_1) \\ \theta_2 &= \theta_r + \pi/6 (f - f_1)/(f_2 - f_1) \\ \phi_1 &= 2\pi/3 (f - f_1)/(f_2 - f_1)\end{aligned}\quad (9)$$

where θ_1 is the receiver takeoff angle.

The average radiation coefficients at frequencies higher than f_2 are assumed to be equal to those calculated at the frequency $f = f_2$. In the numerical tests of the technique presented in this study we used $f_1 = 1$ Hz and $f_2 = 3$ Hz.

Tests of the Method

In this section we present results of several tests that were performed to check the validity of the HGF technique at simulating near-fault ground motion. The tests consist of comparisons with the new ESF method described earlier,

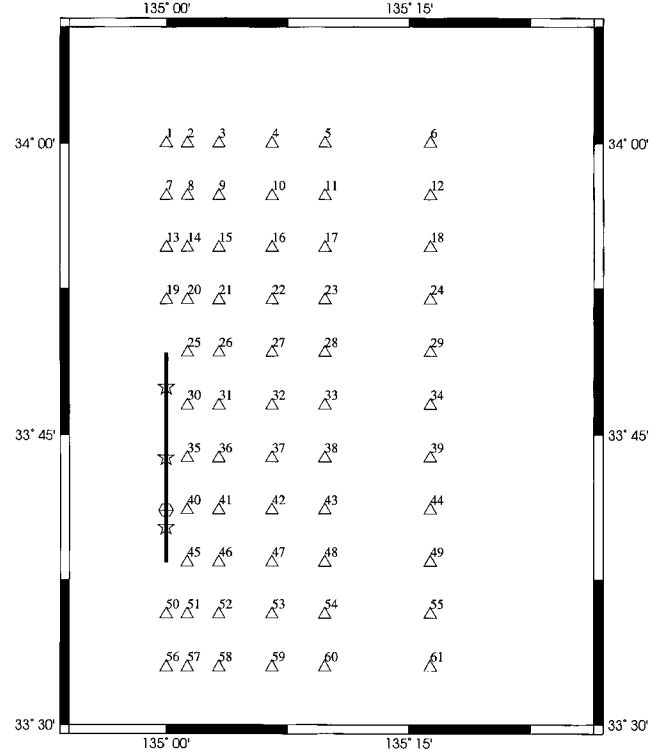


Figure 3. Fault and receiver locations. Stars and diamond indicate the small events and the mainshock epicenters, respectively. The triangles indicate the locations of receivers.

comparisons of synthetic and recorded seismograms, and empirical attenuation relations of strong-ground motion.

Comparison with the ESF Method

We compared synthetic seismograms calculated with the HGF and ESF methods for a M 6.5 earthquake with a pure strike-slip mechanism and a seismic moment $M_0 = 6.31 \times 10^{25}$ dyne cm. The representation of the radiation pattern in the ESF method is done using empirical source functions (Somerville *et al.*, 1991). The method has been tested against strong-motion data from several types of earthquakes and has proven to be very effective for simulating broadband ground motions from large earthquakes (e.g., Cohee *et al.*, 1991; Somerville *et al.*, 1991). Figure 2 shows the stress-drop models used to simulate broadband ground motions at stations regularly distributed around the fault. The fault is buried at 1-km depth, and its length and width are 20 km and 9 km, respectively. Its location and the station configuration are shown in Figure 3. We used a rupture velocity of 2.7 km/sec and a bell-shaped source-time function with a duration of 0.8 sec. In order to avoid additional complexities in the simulated waveforms due to wave-propagation effects the simulations were done with an homogeneous half-space velocity model with $V_p = 5.2$ km/sec, $V_s = 3.0$ km/sec, $\rho_0 = 2.3$ g/cm³ and $Q = 500$. The fault plane was divided into 13×5 subfaults each having an area of 1.54×1.8 km².

The number of subfaults was derived using the scaling relationship expressed by equation (1). In the Green's function simulations we used six subevents regularly distributed on the fault plane. Each of them is of magnitude M 4.6 with seismic moment $M_0 = 1.26 \cdot 10^{23}$ dyne cm.

The low frequency part (< 1 Hz) of the six hybrid Green's functions was calculated using the 1D frequency-wave number technique of Saikia (1994). As in the original scheme of Kamae *et al.* (1998) the response of each subfault is represented by the Green's function corresponding to the closest subevent corrected for the rupture arrival time and geometrical spreading.

In Figures 4 and 5 we compare the distribution of the fault-normal peak acceleration and peak velocity, respectively, calculated with the HGF and ESF methods using the

source model shown in Figure 2(a). In both simulations the low- and high-frequency parts of the synthetic Green's functions are combined by a pair of matching filters with a transition-frequency range at 0.9–1.1 Hz. The methods agree relatively well. The peak-velocity pattern, which is similar in both calculations, reflects the source-directivity effect. Because the rupture starting point is located in the southern part of the fault, the peak velocity is larger at most of the sites located north of epicenter. The difference in peak velocity between the two techniques is on average less than 15% while the difference in peak acceleration is slightly higher at stations very close to the central part of the fault. The near-fault peak-acceleration distribution calculated with HGF is more uniform than that of peak velocity, which is clearly affected by the source directivity. This result is in a

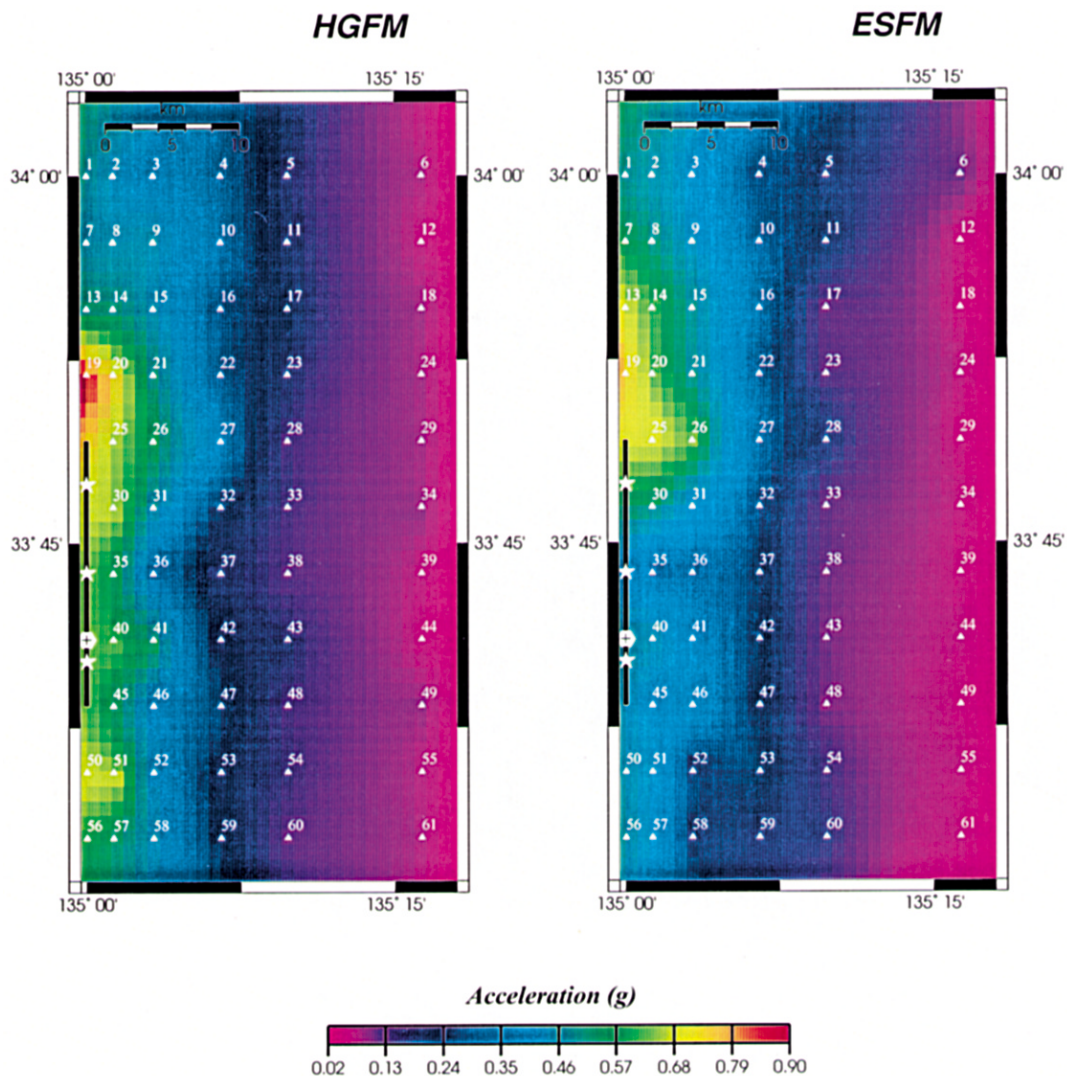


Figure 4. Map of peak acceleration (fault-normal component) distribution calculated with the HGF method (left panel) and the ESF method (right panel) for a M 6.5 strike-slip earthquake. Also shown are the locations of the fault-trace (solid line), stations (triangles), small-events epicenter (stars), and mainshock epicenter (hexagon).

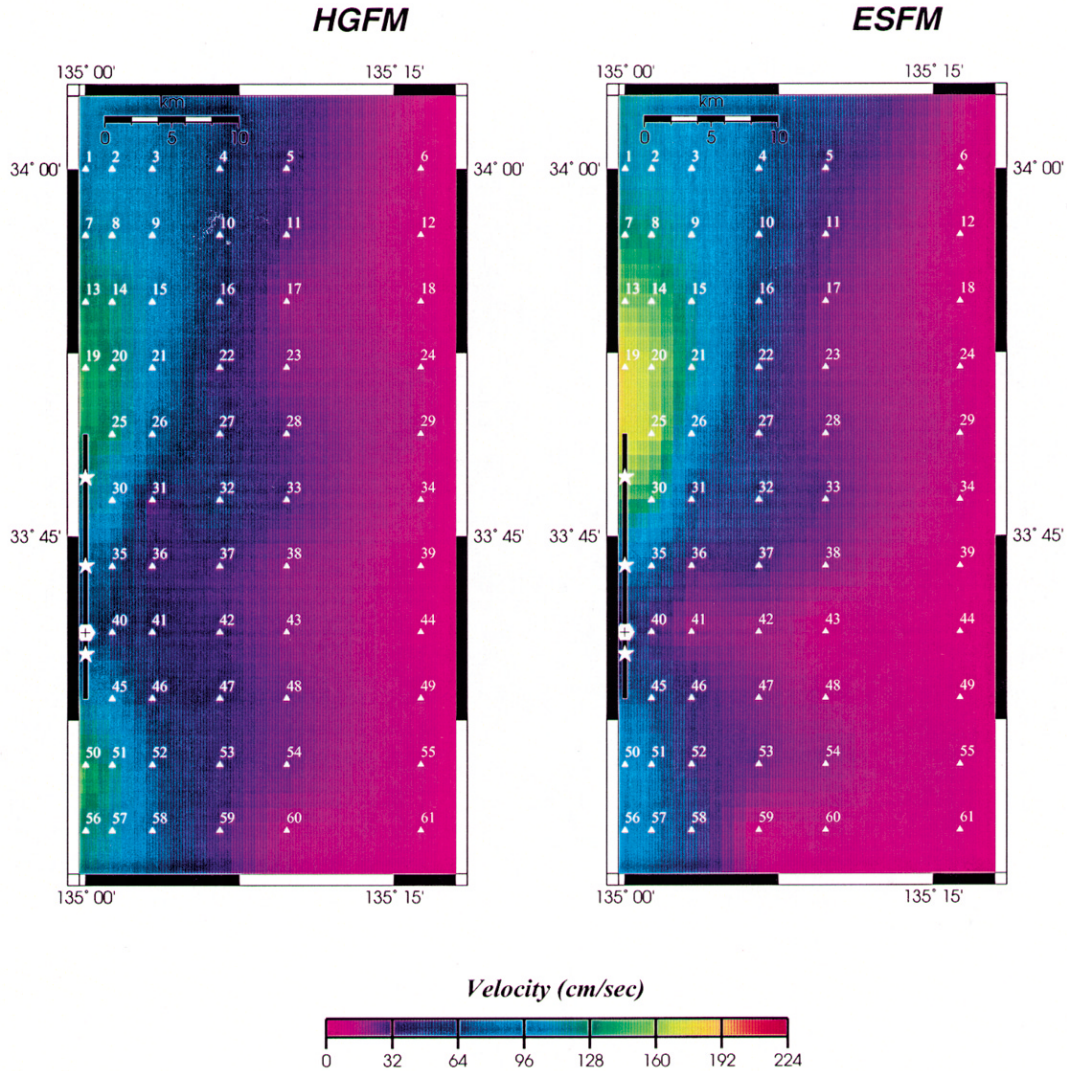


Figure 5. Same as Figure 4, but for the peak velocity.

good agreement with the observation that source directivity does not affect the high frequencies.

Comparisons between synthetic acceleration and velocity waveforms calculated with the two techniques are shown in Figure 6 and Figure 7, respectively. The waveforms and the time duration of the synthetic seismograms are quite similar. The long-period pulses seen at receivers located north of the fault, and the increase in the time duration of the ground motion at receivers located south of the epicenter, are a direct consequence of the source process which is similarly represented in the two techniques. The differences seen in the high-frequency waveforms appearing before the S wave are due to the fact that the high-frequency part of the hybrid Green's functions is calculated only for the S wave.

The limited number of hybrid Green's functions used in this simulation makes the HGF calculation less accurate at sites affected by backward directivity. At these sites the phases representing the energy contribution from each sub-

fault are distinctively lagged in time since the rupture propagates in the opposite direction, away from the stations. Therefore even small differences in the synthetic Green's functions used by the two techniques can have a significant effect on the synthetic waveforms. There is no limitation in the number of hybrid Green's functions used in the proposed technique. Increasing the number of hybrid Green's functions certainly improves the quality of the simulation, but at the expense of the computation time. The choice of the numerical technique used to calculate the hybrid Green's functions as well as their number depends on knowledge of the underground structure and the degree of the source-model complexity.

In Figures 8 and 9 we show the comparison of the acceleration- and velocity-response spectra, respectively, calculated at receivers 1 to 7, which are affected by source directivity. The spectra at these stations compare very well in the period range 0.1 to 10 sec.

(a) Fault–Normal Component

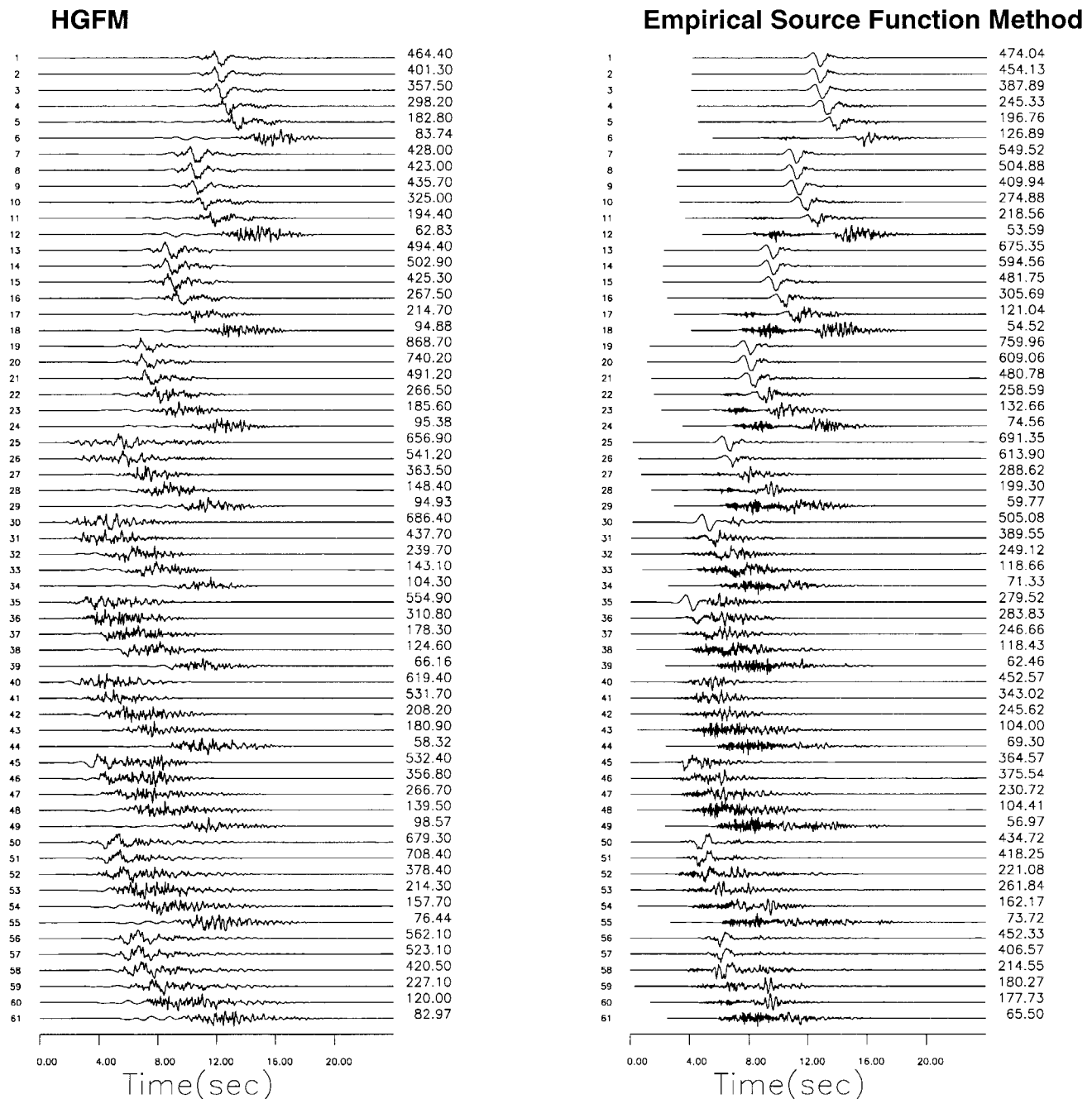


Figure 6. Time histories of the synthetic acceleration (in cm/sec²) calculated at stations shown in Figure 3 using the HGF method (left panel) and the ESF method (right panel) for a M 6.5 strike-slip earthquake. (a) fault-normal component.

We applied the procedure of Abrahamson *et al.* (1990) to measure the goodness of fit of response-spectral acceleration between the ground motions simulated with the two methods. In our experiment the goodness of fit is measured by the bias, which is expressed as a function of period. The bias measures the difference between the two simulations

averaged over all stations at the considered period range. Figure 10 shows the bias and the standard error of residual between the response spectra simulated with the two techniques. The goodness of fit in response-spectral acceleration of the two horizontal components indicates that the bias mean between the two simulations is relatively small, al-

(b) Fault-Parallel Component

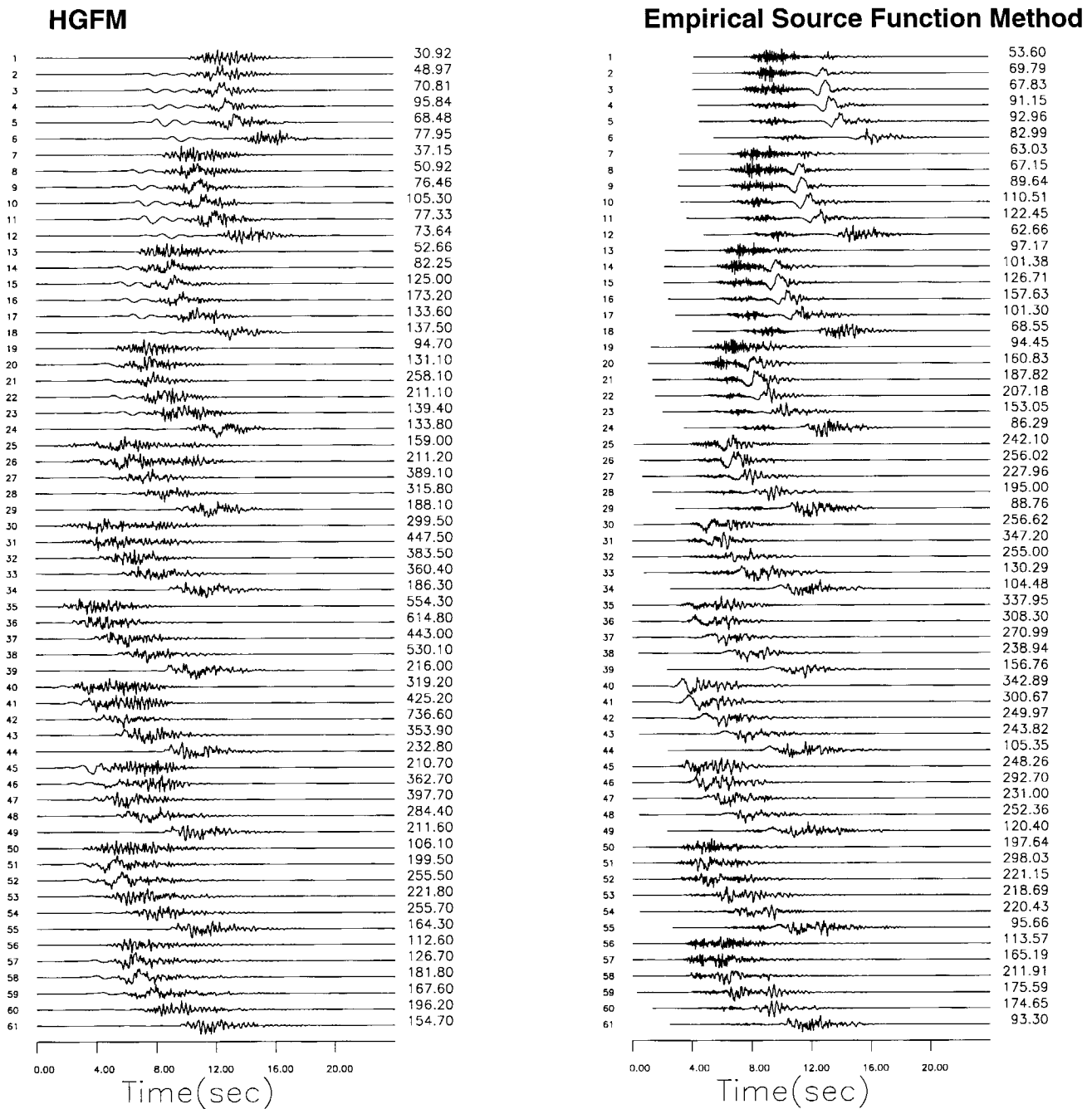


Figure 6. (Continued) (b) fault-parallel component.

though there is a tendency for the HGF method to produce slightly larger ground motions. The bias at long periods and the scattering are greater at stations that see the whole fault plane and are not affected by the rupture directivity. As discussed previously the bias at these stations is attributable to the difference in the number of Green's functions used by the two techniques.

Comparisons with Empirical Response Spectral Acceleration Models

The performance of the HGF technique was tested by comparing simulated- and empirical-response spectra for rock sites using the Abrahamson and Silva (1997) model for strike-slip earthquakes of M 6.5. The empirical relation of

(c) Vertical Component

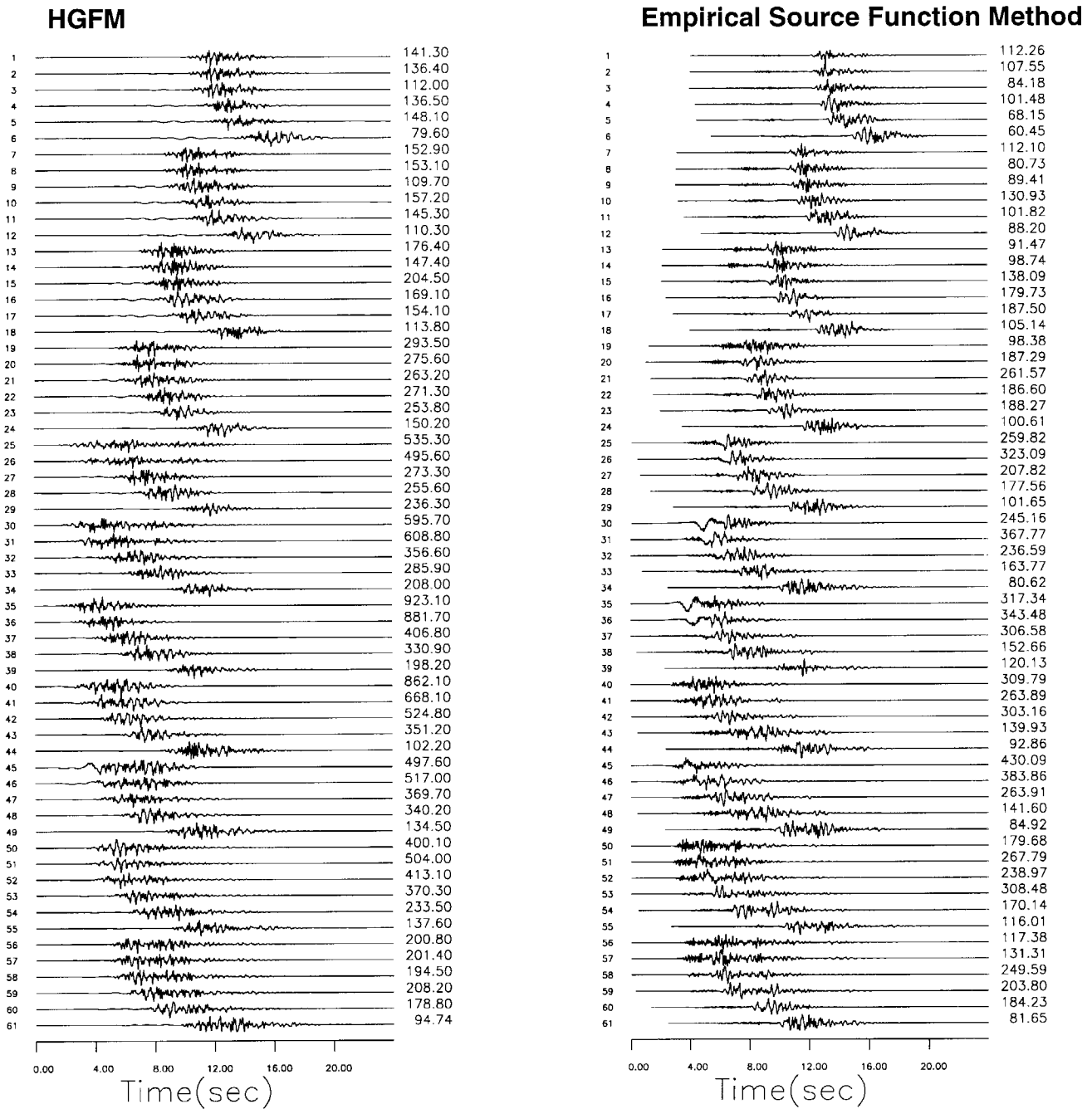


Figure 6. (Continued) (c) vertical component.

Abrahamson and Silva for crustal earthquakes was derived using a worldwide data set of shallow events. According to their soil classification, sites with shear-wave velocity higher than 600 m/sec are considered as rock. We chose M 6.5 for the comparison because it is constrained by the largest amount of data.

Figure 11 shows the comparisons of simulated and empirical peak-ground-acceleration attenuation, and spectral-

acceleration attenuation at several periods. The synthetic accelerations were obtained based on the simulation described in the previous section (white circles) using the source model shown in Figure 2(a) and a second simulation (black circles) using the source model shown in Figure 2(b). In general the simulated accelerations fall within the range of one standard deviation in the empirical model for all the rupture distances and periods except for 2 sec. At this period the simulations

(a) Fault–Normal Component

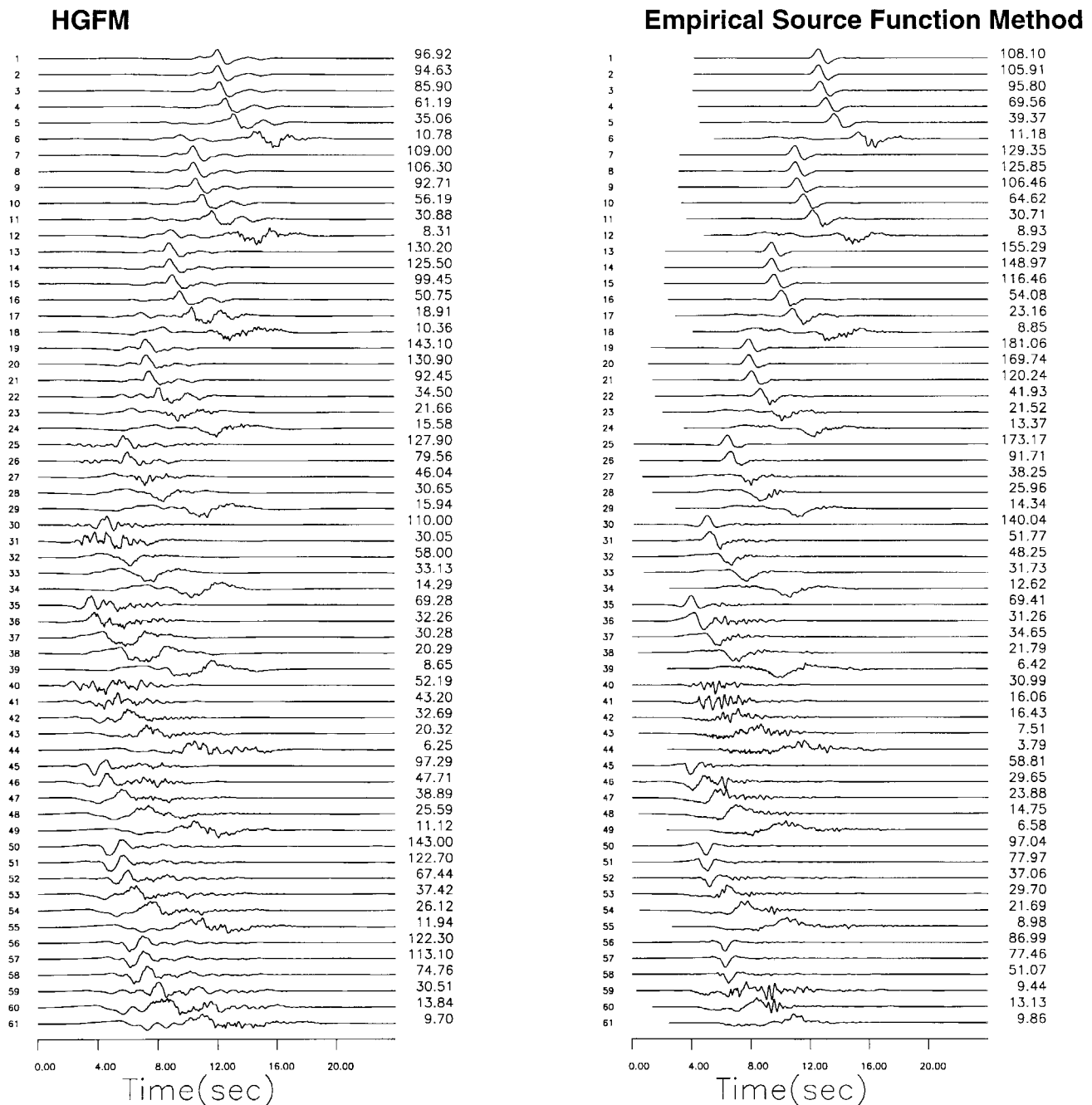


Figure 7. Same as Figure 6, but for the velocity (units are cm/sec).

give slightly larger amplitudes at some of the stations located within the rupture distance range of 5–20 km. We attribute this discrepancy to the directivity effect, which is particularly strong at stations located north of the epicenter in the case of the first simulation and above the hypocenter in the case of the second simulation. The effect of the directivity on simulated ground motions is also seen when we compare the results from the two source models (see Fig. 11). Both

models give comparable peak accelerations at periods shorter than 1 sec. At periods of 1 and 2 sec the first model produces stronger directivity giving slightly larger amplitudes at most of the stations.

The same source representation and matching filters, described in the previous section, were used to compare the simulated average horizontal spectral accelerations and the median predicted by Abrahamson and Silva's (1997) model

(b) Fault-Parallel Component

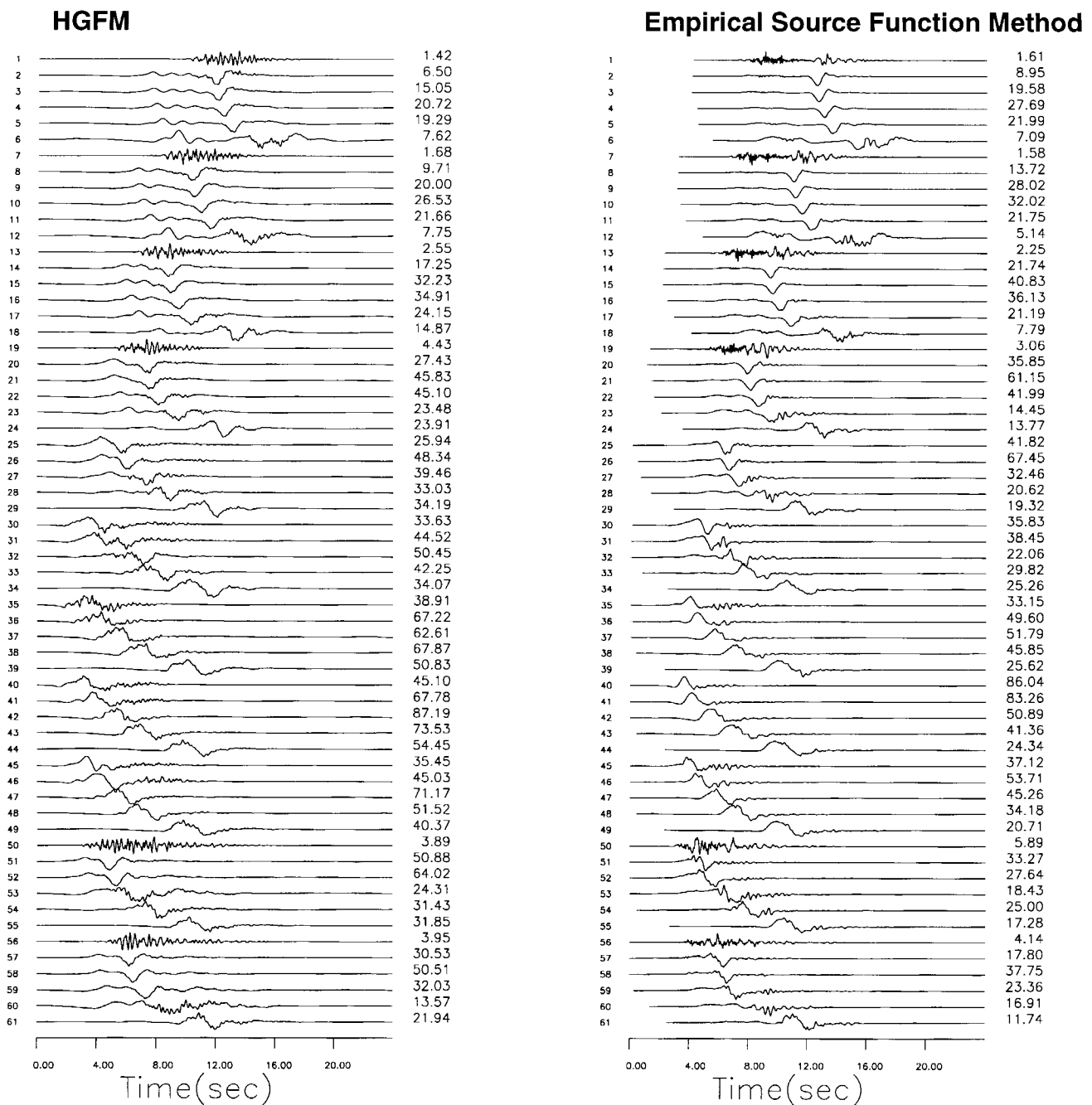


Figure 7. (Continued).

for rock sites at a distance from the rupture of 10 km (Fig. 12). For this comparison, we generated synthetic ground motion at 11 stations located around the fault with a distance from the rupture of approximately 10 km. We used the 1D velocity model shown in Table 1 to calculate the synthetic Green's functions. In this model the shear-wave velocity in the upper 100 m is 1.2 km/sec. The synthetic ground motions were calculated with three different source models, allowing

us to investigate the effect of the source on the simulated spectral acceleration at long periods. Although the empirical response spectral acceleration is based on data from a wide range of strike-slip earthquakes, the comparison with our synthetic spectra derived from a single realization for each source model is good, especially at periods smaller than 1 sec. This is partly due to the fact that the high-frequency part of the near-fault ground motion is less sensitive to the large-

(c) Vertical Component

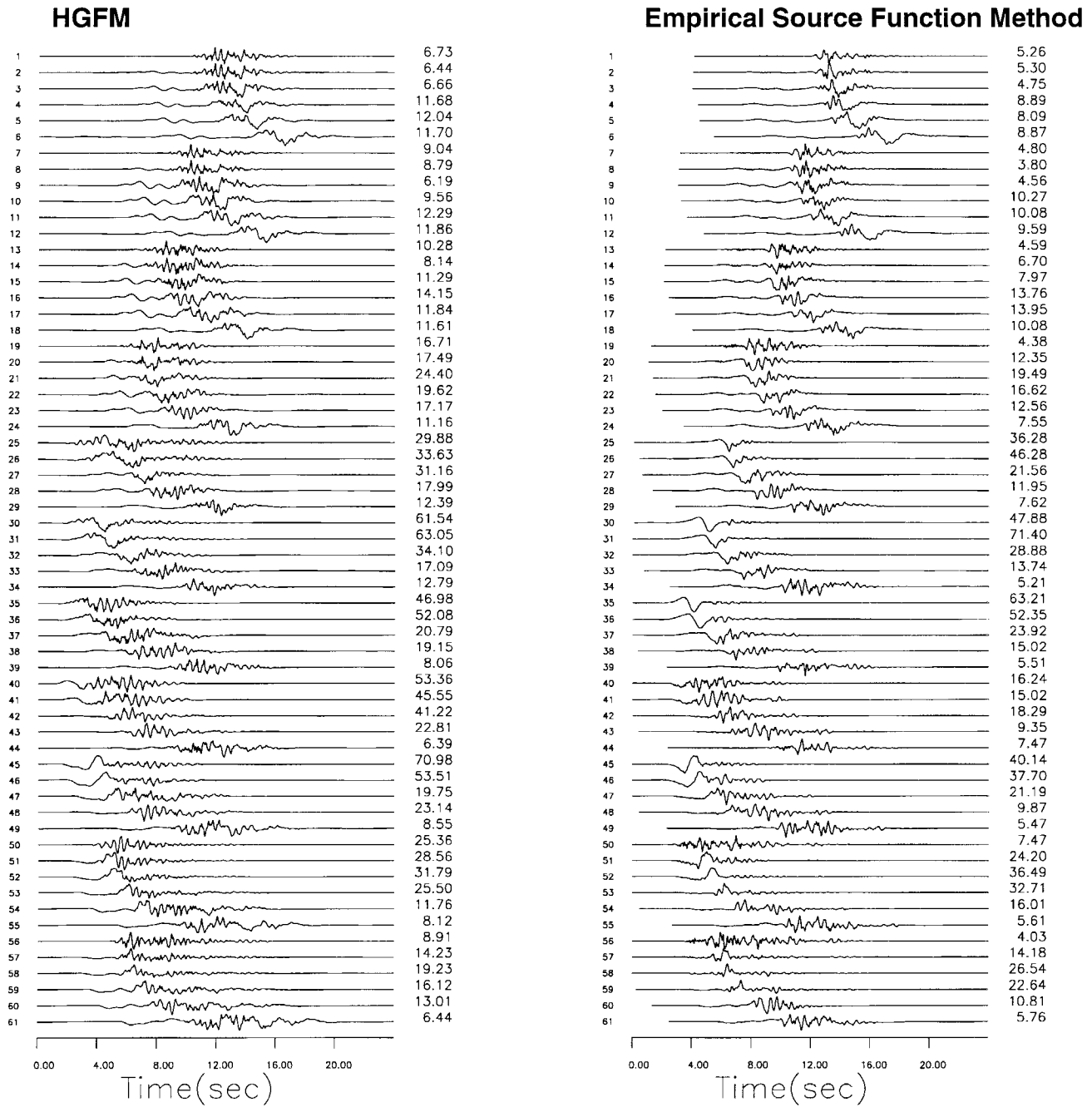


Figure 7. (Continued).

scale complexities in the rupture process. The peak at around 0.2 sec and the quick fall-off of the spectrum at periods shorter or longer than this value are matched very well. At periods longer than 1 sec the simulations give higher response-spectral accelerations. The comparison between the three models suggest that the response at these periods is mainly controlled by the large-scale features of the source model. Model II and Model III that contain multiple

smoothed asperities give better results. The relatively large and smooth asperity in Model I, the location of the rupture starting point, and the pure strike-slip mechanism enhance the directivity effect, which is strong at periods longer than 1 sec at most of the stations. Numerical experiments (e.g., Graves, 1998) performed with several source models suggest that rough and multiple asperities tend to diminish the coherency of long-period energy release during the fault rup-

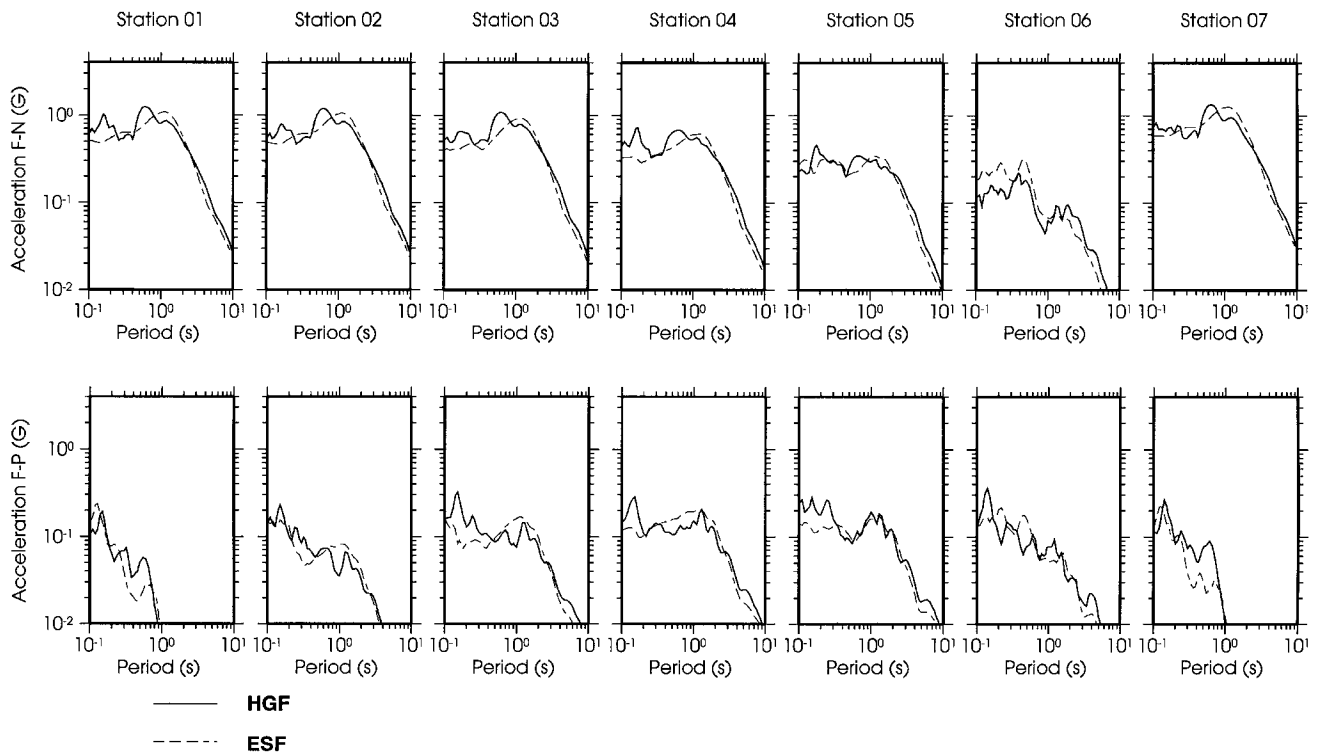


Figure 8. Comparison of acceleration response spectra calculated at seven stations using the HGF method (solid line) and the ESF method (dashed line).

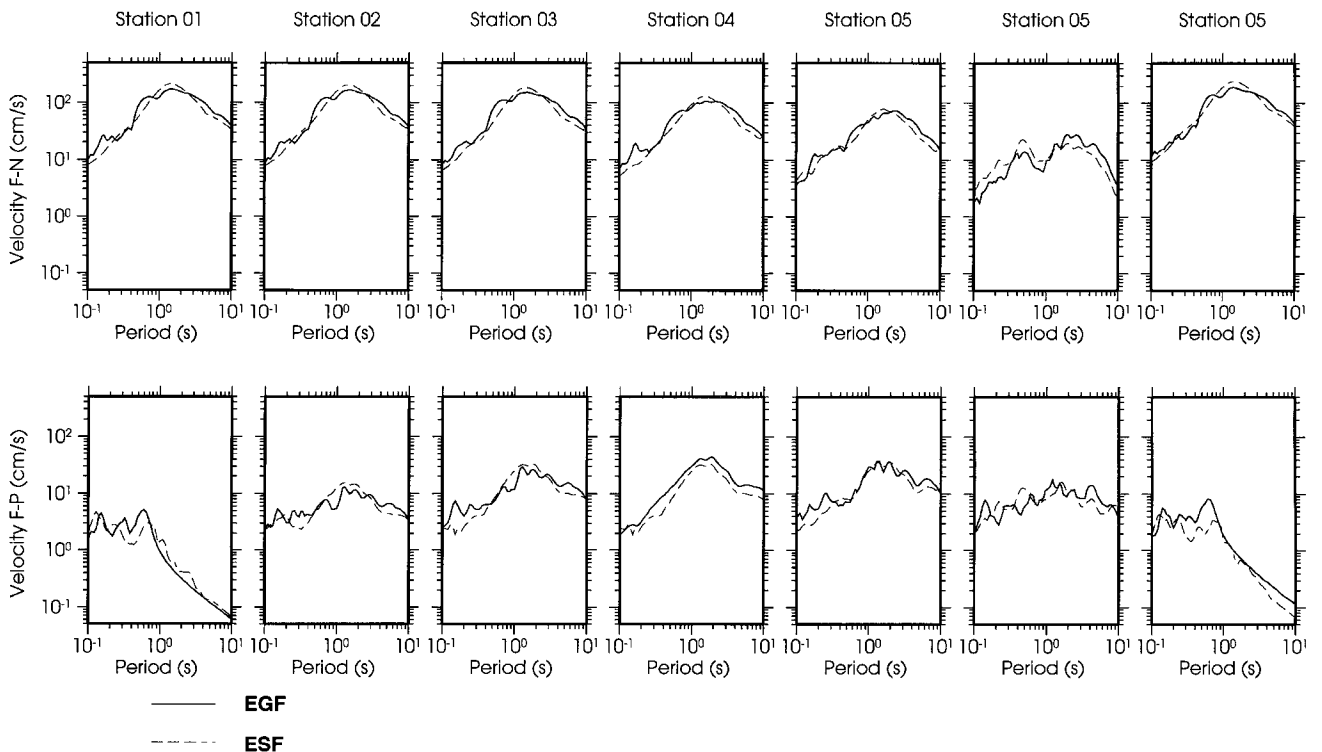


Figure 9. Same as Figure 8, but for the velocity response spectra (5% damping).

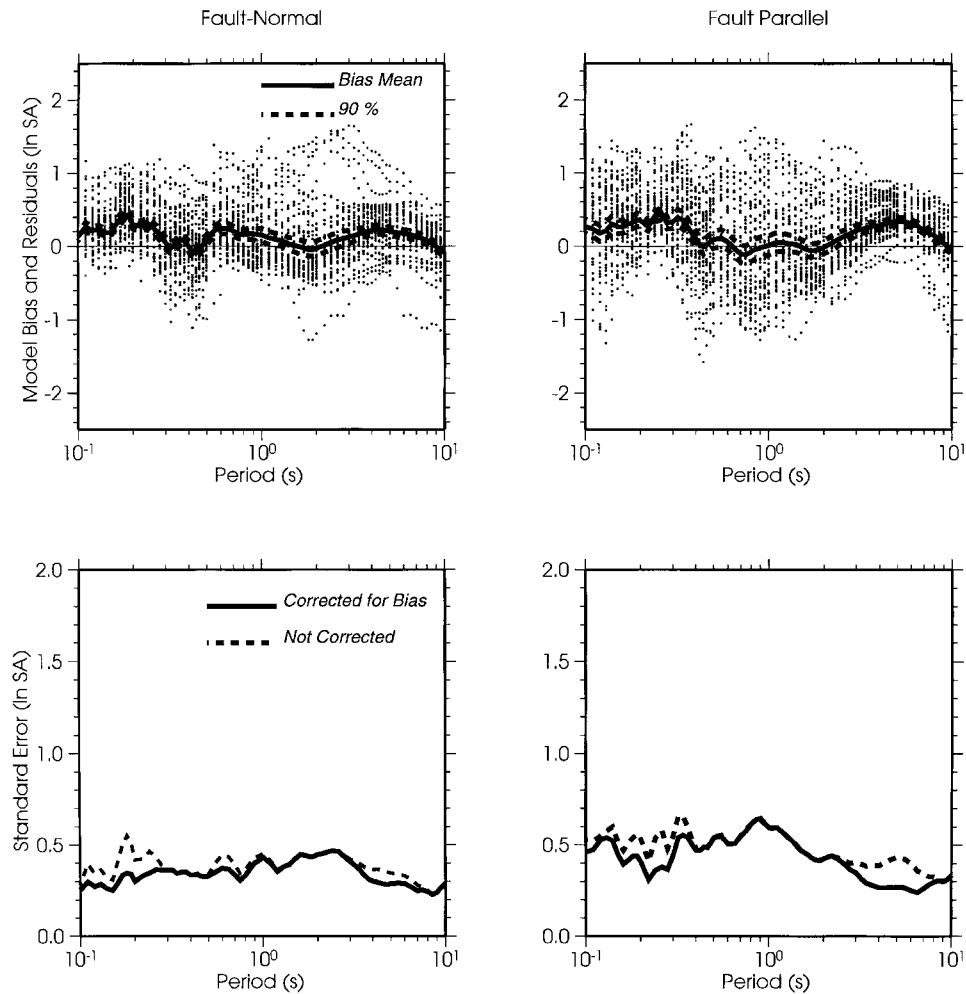


Figure 10. Upper panels: Model bias (solid line) of the natural logarithm of spectral acceleration (reflecting average ratio of synthetic ground motion simulated with HGF and ESF methods), and its 90% confidence interval (dashed lines) at stations shown in Figure 3. A positive bias indicates that the HGF method gives larger ground motion than the ESF method. Lower panel: Standard error of residual between the response spectra obtained with the two techniques, with and without correction for model bias, for the fault-normal component (left panels) and fault-parallel component (right panels).

ture. Consequently they produce weaker near-fault ground motions.

Our result suggests that in order to increase the effectiveness of the HGF technique at simulating ground motions from scenario earthquakes it is necessary to systematically span the range of possible slip models. The departure from the empirical model at stations affected by rupture directivity can be significant for smooth asperity source models.

Simulation of Near-Fault Ground Motion from the 1995 Kobe Earthquake

We applied the HGF method to simulate records of near-fault ground motion from the 1995 Kobe earthquake. The location of the fault and five stations considered in this study

are shown in Figure 13. Among these stations, only KBU is a rock site (Table 2). The basin depth varies from about 600 m beneath KOB and MOT, which are located very close to the basin edge, to 1.3 km beneath TKT and FKA. A schematic view of the fault model used in the simulation is shown in Figure 14. The model has the following features, proposed by Kamae *et al.* (1998). It includes four square-shaped asperities. The stress drop is assumed to be variable within each asperity and zero in the other regions of the fault. The location of the asperities roughly corresponds to the areas of large slip concentration derived from inversions of strong-motion data (e.g. Sekiguchi *et al.*, 1996; Wald, 1996). We found that small modifications of the fourth asperity area do not affect significantly the ground motion at sites considered here. This can be explained by the fact that the sites are

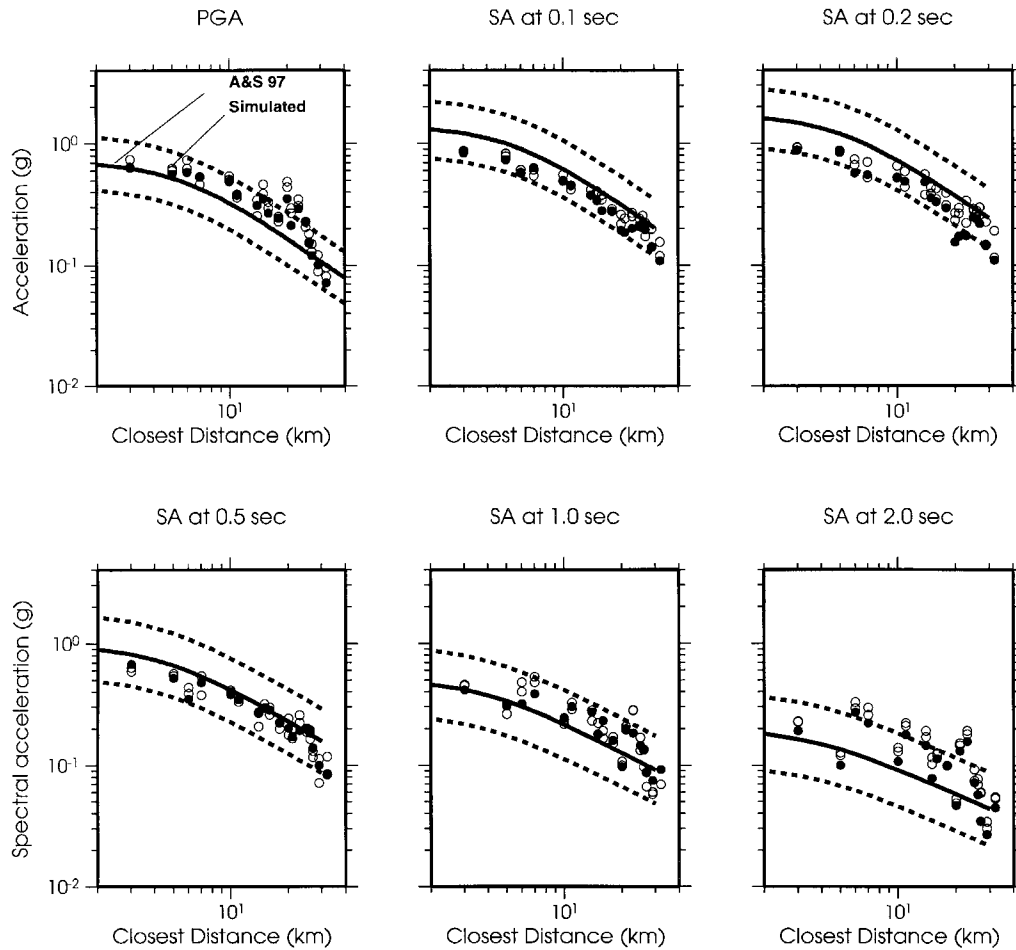


Figure 11. Comparisons of simulated (circles) and empirical peak ground acceleration and spectral acceleration attenuation (solid line) of Abrahamson and Silva (1997), for a M 6.5 strike-slip earthquake. Dashed line is the standard deviation of the empirical attenuation. The simulated accelerations were obtained using the source models shown in Figure 2(a) (white circles) and Figure 2(b) (black circles).

located outside the area affected by the forward-source directivity caused by the rupture of the fourth asperity.

Hybrid Green's functions are calculated for four point sources located at the center of each asperity assuming a magnitude 4.7 for each source. The source parameters for the M 4.7 small event are summarized in Table 3. We used 1D and 3D techniques to simulate the low-frequency part (0.1–1 Hz) of the Green's function and the stochastic technique of Boore (1983) for the high-frequency part (>1 Hz). The transition-frequency range in the matching filters was 0.9–1.1 Hz.

Pitarka *et al.* (1998) found that, at long periods, the local bedrock geometry does not have a significant effect at KOB and MOT, while it has an impact at TKT and FKA. According to Kamae *et al.* (1998), who tested the 3D versus 1D effect at the basin sites considered in this study, the effect of the thin shallow sedimentary layers is significant at frequencies around 1 Hz. Based on these results, we used 1D

velocity models to calculate the low-frequency part of the Green's functions at KBU, KOB, and MOT (Table 4), and the 3D velocity model of Pitarka *et al.* (1998) for TKT and FKA. In the 3D calculations we used a variable-grid finite-difference scheme (Pitarka, 1999). The velocity model was discretized with a grid spacing of 60 m in the horizontal direction, and 60 m, 100 m, 200 m, 300 m, and 400 m in the depth intervals of 0–1 km, 1–2 km, 2–5 km, 5–8 km, and 8–24 km, respectively.

The simulated and observed velocity and acceleration seismograms at KBU, KOB, and MOT are depicted in Figure 15. Except for the fault-normal component of acceleration at KOB, there is a good agreement in the peak velocity and acceleration at all sites. The agreement between the simulated and recorded acceleration waveforms is fair and that of the velocity waveforms is relatively good. The observed long-period pulses are well simulated.

The comparison at TKT and FKA is shown in Figure

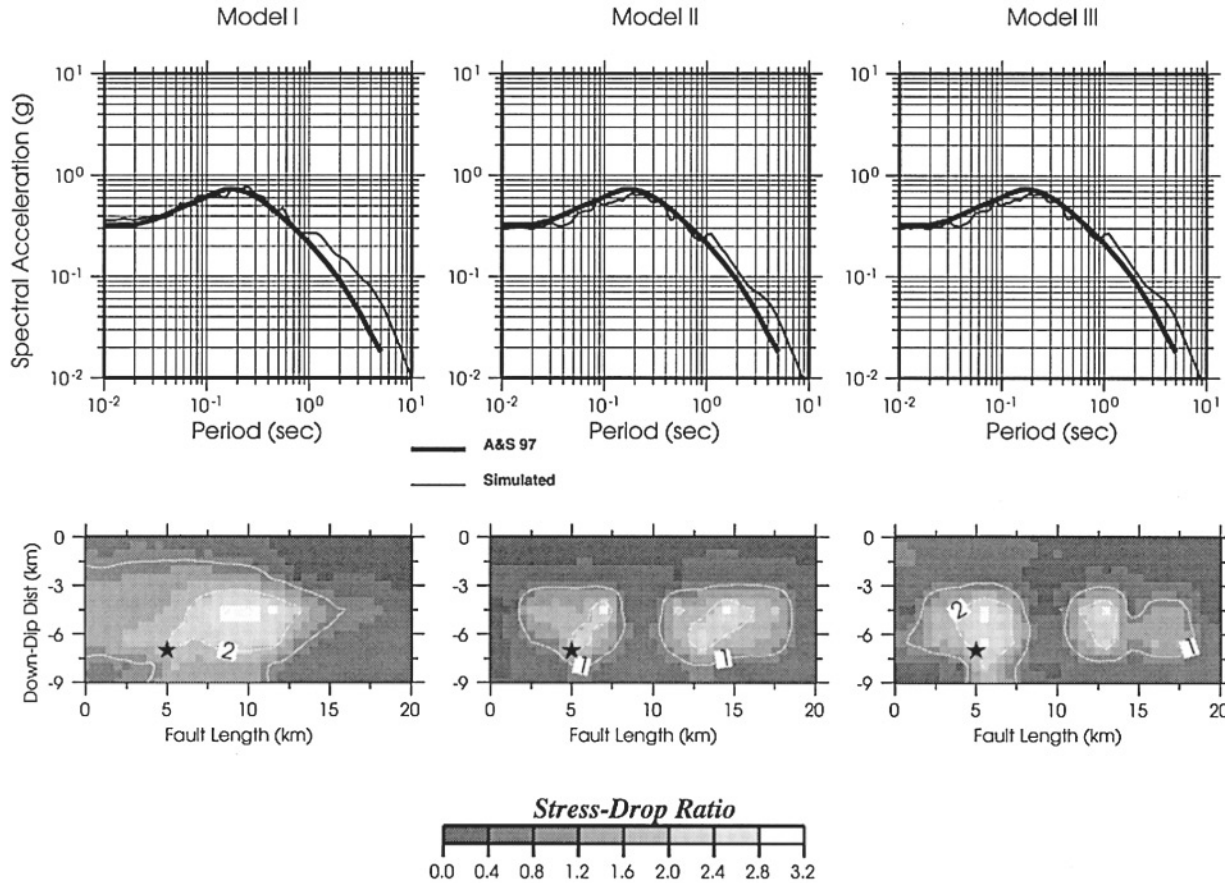


Figure 12. Comparisons of simulated (thin line) and empirical (thick line) spectral acceleration of Abrahamson and Silva (1997) at a rupture distance of 10 km for a M 6.5 strike-slip earthquake. The simulations were done using three different source models shown in the lower panels.

Table 1
Velocity Model for Rock Sites

Depth (km)	V_p (km/sec)	V_s (km/sec)	Density (g/cm^3)	Q_p	Q_s
0.10	2.4	1.2	2.0	100	50
1.25	3.5	2.0	2.1	200	100
4.45	4.4	2.5	2.2	500	300
>4.45	5.7	3.5	2.3	500	300

16. It is obvious that the complexities in the waveforms observed at these sites are related not only to the source process, but also to the basin-edge effect and the surface-sedimentary-layer response. Our simulation reproduces well the duration and the first part of the ground motion, which is mainly affected by the rupture directivity and to a lesser extent by the basin edge effect. We interpret the second large pulse seen in both sites as a superposition of waves coming

directly from the fourth asperity and surface waves generated at the basin edge. The later phases in the acceleration observed at TKT suggest that the response of the shallow sediments during the mainshock was nonlinear. They were not reproduced by our elastic technique. Aguirre and Irikura (1997), who modeled the response of reclaimed land sites in the Kobe region, concluded that the response of soft sediments throughout the damaged region may have been nonlinear during the mainshock.

Conclusions

The HGF method is designed to combine the advantages of both deterministic and stochastic approaches and has the flexibility of incorporating complexities in the source, wave-path, and local site effects into strong ground motion simulation. It is sometimes argued that the effects of the source and path must be averaged over various scenarios in pre-

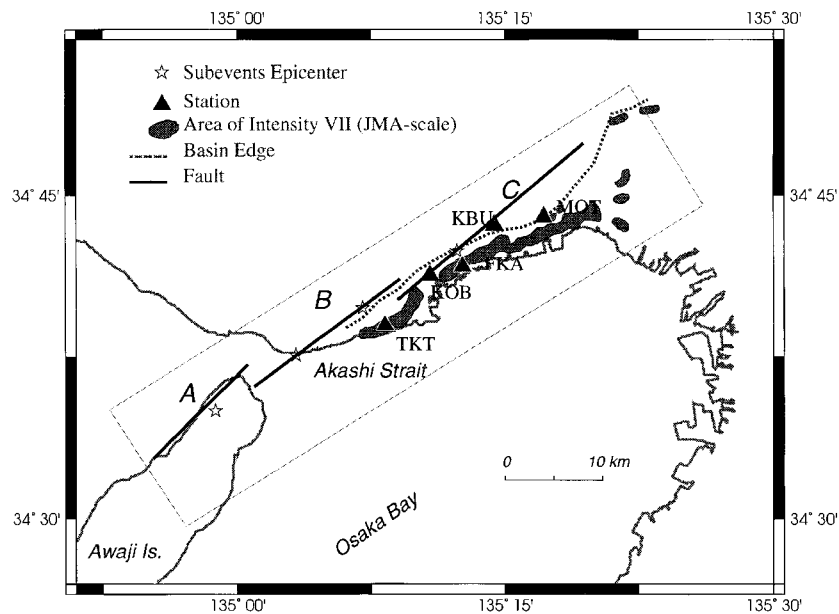


Figure 13. Map of Kobe area and station locations. The rectangle shows the areal extent of the basin model used in the 3D simulations of the Green's functions. Also shown are the locations of the damaged zone and epicenters of four hypothetical small events (stars).

Table 2
Station Locations

Station Name	Lat. (deg.)	Long. (deg.)	Geological Conditions
KBU	34.725	135.240	Soft Rock
KOB	34.688	135.180	Alluvium
MOT	34.725	135.281	Alluvium
TKT	34.649	135.138	Alluvium
FKA	34.695	135.211	Alluvium

dicting ground motion for seismic design, so the HGF method may not perform better than simpler techniques that represent the time history of the ground motion using the stochastic approach. This is not quite true in the case of near-fault ground motion, especially that affected by source directivity and basin-edge geometry. Records of near-fault ground motion from 1989 Loma Prieta, 1992 Landers, 1994 Northridge, and 1995 Kobe earthquakes demonstrate that most of the seismic energy is carried by long-period waves generated by source directivity and affected by the wave path (e.g., Steidl *et al.*, 1991; Wald *et al.*, 1991; Cohe and Beroza, 1994; Olsen and Archuleta, 1996; Somerville *et al.* 1996; Kamae and Irikura, 1998). Such ground motions cannot be well represented by stochastic models in time domain. The long-period characteristics of near-fault ground motion have a significant impact on the dynamic response of large structures. Current research on the dynamic response of

structures to near-fault ground motions relies heavily on nonlinear dynamic analysis using ground-motion time histories as input. This requires the use of several strong-motion seismograms, recorded or simulated, each of which is the realization of a single scenario that incorporates particular source and wave-path effects at low frequencies. For this purpose it is not meaningful to use a ground-motion time history that represents the average of multiple scenarios. The HGF method is designed to fulfill such a requirement, including the effect of the coherence of the source radiation pattern, which is at the origin of the source-directivity effect. We believe that the period, amplitude, and timing of the long-period phases that often characterize near-fault ground motion are of primary importance for building design, and that the improvement of numerical techniques and knowledge of underground structure are needed for the development of methods that apply a deterministic approach to near-fault ground-motion prediction.

Although it occupies a narrow-frequency range, the inclusion of the frequency-dependent radiation-pattern effect into broadband near-fault ground-motion simulations provides an important enhancement of the method. The simplistic representation of the radiation-pattern effect by constant coefficients usually applied in broadband simulations may produce unrealistic synthetic seismograms. Studies of the radiation-pattern effect in a broad-frequency range based on ground-motion data are necessary to understand the frequency dependence of the source radiation and its effect in near-fault ground motion.

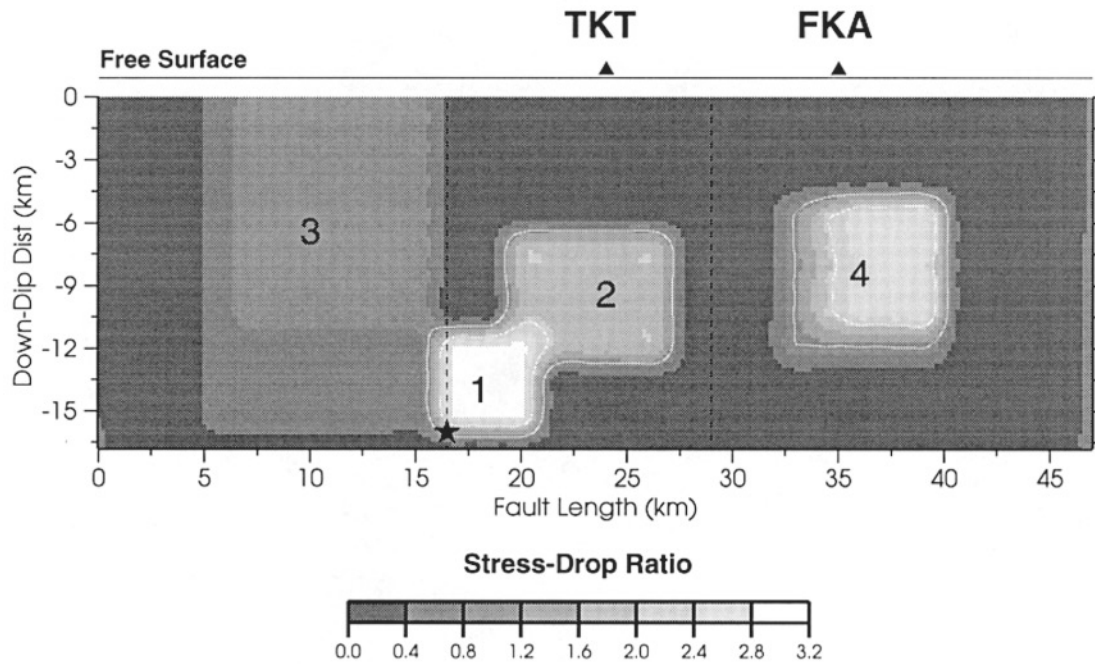


Figure 14. Source model consisting of four rectangle-shaped asperities. The stress drop ratio within the asperities is estimated by the forward modeling of near-fault ground motion.

Table 3
Source Parameters for M 4.7 Small Event

Seismic Movement (dyne cm)	1.30×10^{23}
Corner Frequency (Hz)	1.3
Focal Mechanism	strike 53°; dip 90°; rake 180°
Rise Time (sec)	0.12

Table 4
One-Dimensional Velocity Models

Site	Depth (km)	V_p (km/sec)	V_s (km/sec)	Density (g/cm^3)	Q_p	Q_s
KBU	0.5	3.2	1.8	2.0	500	300
KBU	5.0	5.7	3.2	2.4	1000	400
KBU	>5.0	6.0	3.46	2.7	1000	500
MOT	0.035	1.5	0.3	1.9	130	50
MOT	0.05	1.7	0.45	1.9	150	80
MOT	0.15	1.8	0.50	2.0	150	80
MOT	0.30	1.8	0.65	2.0	150	80
MOT	0.6	1.9	1.1	2.2	300	170
MOT	5.0	5.7	3.2	2.4	1000	400
MOT	>5.0	6.0	3.46	2.7	1000	500
KOB	0.06	1.5	0.45	1.9	150	80
KOB	0.2	1.7	0.55	2.0	150	80
KOB	0.4	1.8	0.65	2.0	150	80
KOB	0.6	1.9	1.1	2.2	300	170
KOB	5.0	5.7	3.2	2.4	1000	400
KOB	>5.0	6.0	3.46	2.7	1000	500

The generally good agreement between simulated and recorded ground motion obtained for the 1995 Kobe earthquake and shown in this study indicates that the technique has the capability of reproducing the main characteristics of near-fault ground motion from basin-edge faults. At sites where the nonlinear effect of sediments is preponderant, the technique needs to be augmented by nonlinear techniques. Numerical experiments indicate that the summation of Green's functions using the technique proposed by Irikura and Kamae (1994) performs relatively well when the seismic source is characterized by well-distinguished large asperities, as it is the case of the Kobe, Japan, earthquake.

Acknowledgments

Discussions with K. Kamae and T. Sato are greatly appreciated. We thank G. Atkinson and an anonymous reviewer for their valuable suggestions. This work was partially supported by TEPCO, Japan.

References

- Abrahamson, N. A., P. G. Somerville, and C. Allin Cornell (1990). Uncertainty in numerical strong motion predictions, in *Proc. 4th Nat. U.S. Conference Earthquake Engineering (Palm Springs)*, *Earthquake Eng. Res. Inst.* **1**, 407–416.
- Abrahamson, N. A., and W. J. Silva (1997). Empirical response spectral attenuation relations for shallow crustal earthquakes, *Seism. Res. Lett.* **68**, 94–127.
- Aguirre, J., and K. Irikura (1997). Nonlinearity, liquefaction, and velocity

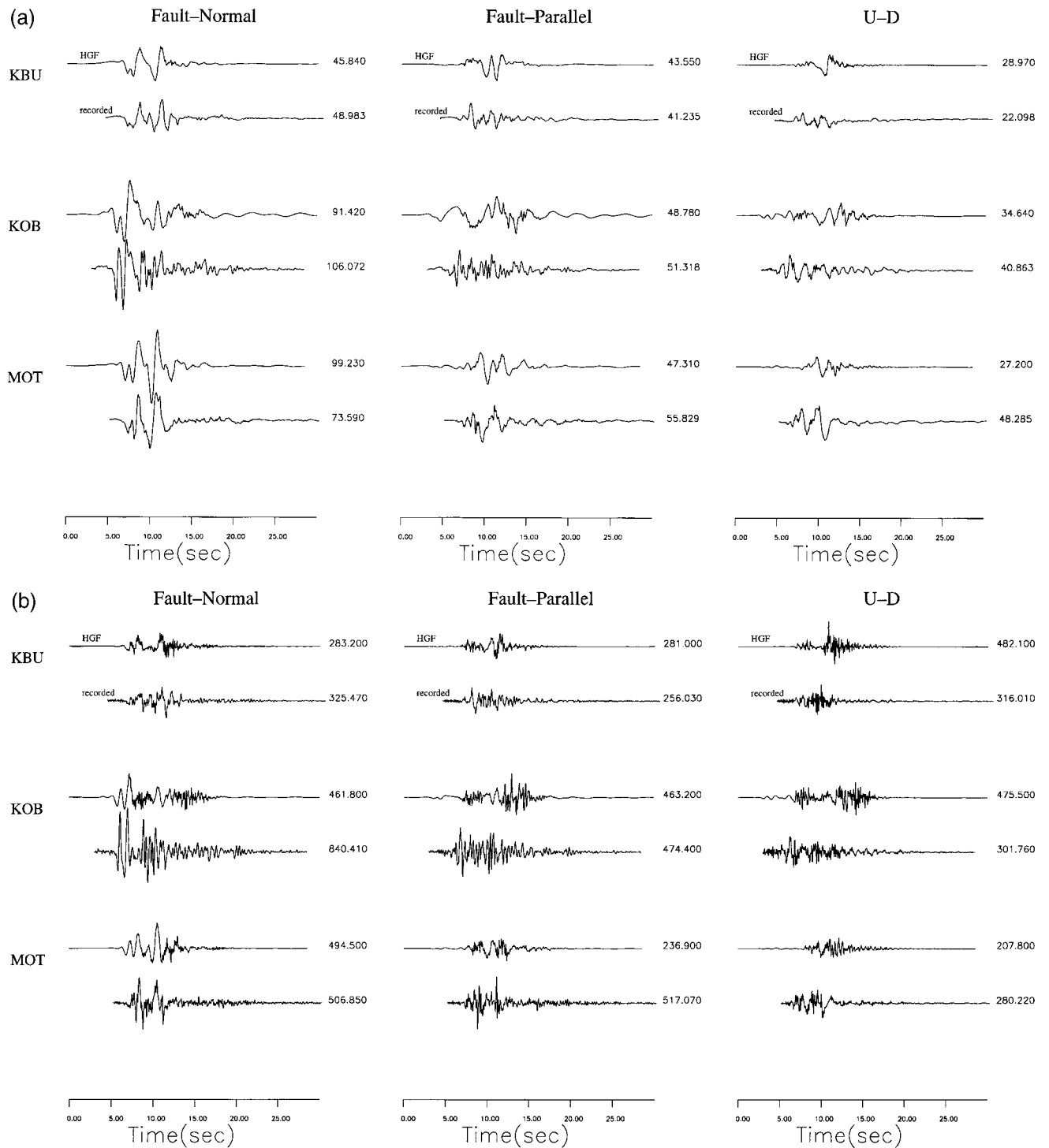


Figure 15. Comparison of synthetic (upper trace) and recorded (lower trace) time histories of the ground motion at KBU, KOB, and MOT. (a) Velocity: the number to the right of each trace gives its maximum amplitude in cm/sec (b) acceleration: the number to the right of each trace gives its maximum amplitude in cm/sec².

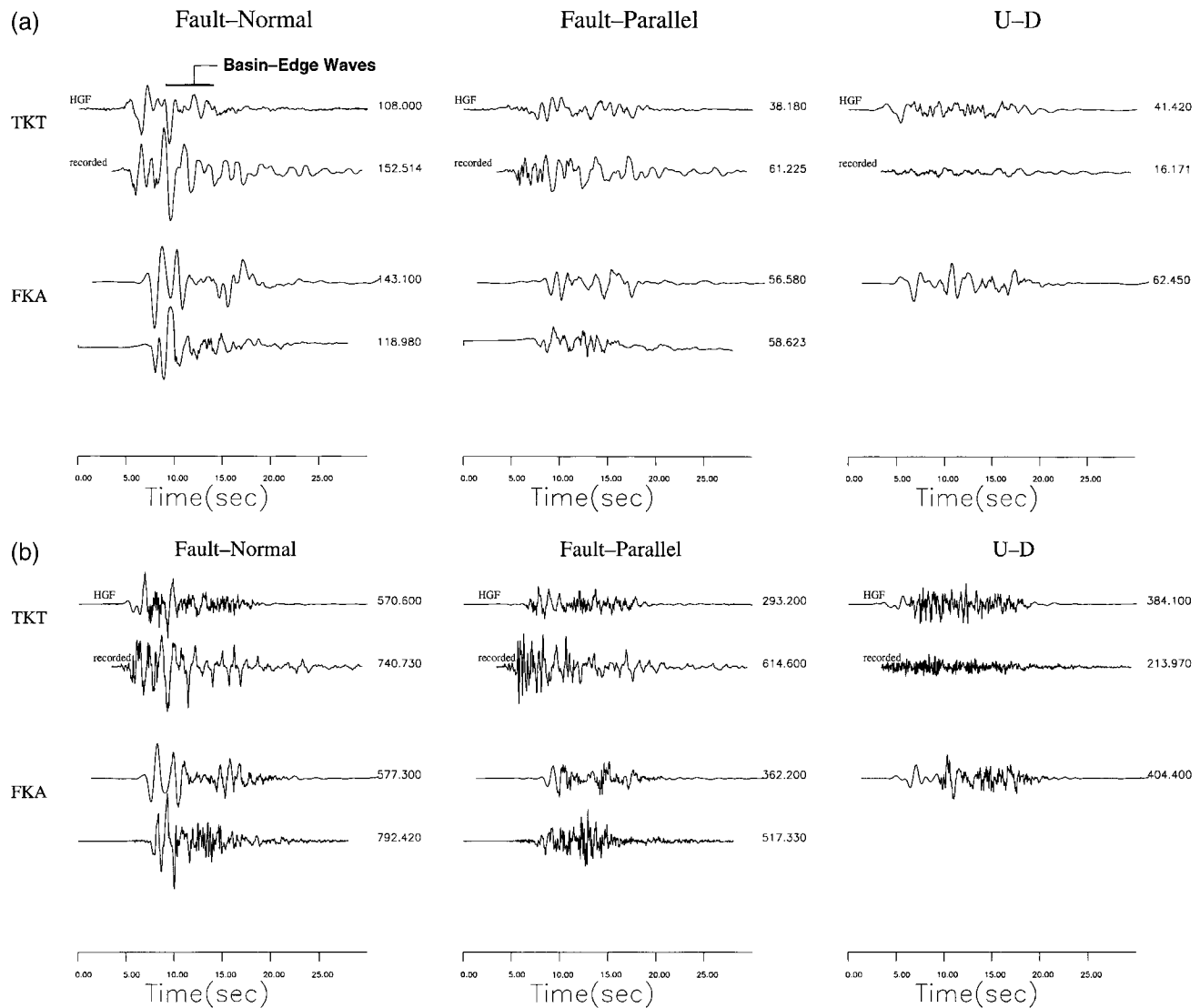


Figure 16. Same as Figure 15, but for TKT and FKA.

variation of soft soil layers in Port Island, Kobe, during the Hyogoken Nanbu earthquake, *Bull. Seism. Soc. Am.* **87**, 1244–1258.

- Atkinson, G. M., and W. Silva (1997). An empirical study of earthquake source spectra for California earthquakes, *Bull. Seism. Soc. Am.* **87**, 97–111.
- Beresnev, I. A., and G. M. Atkinson (1998). Stochastic finite-fault modeling of ground motions from the 1994 Northridge, California, earthquake. I. Validation on rock sites, *Bull. Seism. Soc. Am.* **88**, 1392–1401.
- Boore, D. M. (1983). Stochastic simulation of high-frequency ground motions based on seismological models of the radiated spectra, *Bull. Seism. Soc. Am.* **73**, 1865–1894.
- Boore, D. M., and J. Boatwright (1984). Average body-wave radiation coefficients, *Bull. Seism. Soc. Am.* **74**, 1615–1621.
- Brune, J. (1970). Tectonic stress and the spectra of seismic shear waves from earthquakes, *J. Geophys. Res.* **75**, 4997–5009.
- Chin, B. H., and K. Aki (1991). Simultaneous study of the source, path and site effects on strong ground motion during the 1989 Loma Prieta earthquake: a preliminary result on pervasive nonlinear site effects, *Bull. Seism. Soc. Am.* **81**, 1859–1884.
- Cohee, B. P., and G. C. Beroza (1994). Slip distribution of the 1992 Landers

earthquake and its implications for earthquake source mechanics, *Bull. Seism. Soc. Am.* **84**, 692–712.

- Cohee, B. P., P. G. Somerville, and N. A. Abrahamson (1991). Simulated ground motion for hypothesized $M_w = 8$ subduction earthquakes in Washington and Oregon, *Bull. Seism. Soc. Am.* **81**, 28–56.
- Frankel, A. (1995). Simulating strong motion of large earthquakes using recordings of small earthquakes: the Loma Prieta Mainshock as a test case, *Bull. Seism. Soc. Am.* **85**, 1144–1160.
- Graves, R. W. (1998). 3D finite-difference modeling of the San Andreas Fault: source parameterization and ground motion levels, *Bull. Seism. Soc. Am.* **88**, 881–897.
- Graves, R. W., P. G. Somerville, and N. F. Smith (1996). Simulated broadband strong motion time histories throughout Osaka Prefecture for five faults beneath and bounding Osaka basin, including near-fault rupture directivity and 3D basin response effects, Report to Georesearch Institute, Osaka, Japan.
- Hadley, D. M., D. V. Helmberger, and J. A. Orcutt (1982). Peak acceleration scaling studies, *Bull. Seism. Soc. Am.* **72**, 959–979.
- Hanks, T., and R. McGuire (1981). The character of high-frequency strong ground motion, *Bull. Seism. Soc. Am.* **71**, 2071–2095.

- Hartzell, S. H. (1978). Earthquake aftershocks as Green's functions, *Geophys. Res. Lett.* **5**, 1–4.
- Hartzell, S., S. Harmsen, A. Frankel, and S. Larsen (1999). Calculation of broadband time histories of ground motion: comparison of methods and validation using strong-ground motion from the 1994 Northridge earthquake, *Bull. Seism. Soc. Am.* **89**, 1484–1504.
- Irikura, K., and K. Kamae (1994). Estimation of strong ground motion in broad-frequency band based on a seismic source scaling model and an empirical Green's function technique, *Annali di Geofisica xxxvii*, **6**, 1721–1743.
- Joyner, W. B., and D. M. Boore (1986). On simulating large earthquakes by Green's function addition of smaller earthquakes, in *Earthquake Source Mechanics, Maurice Ewing Series 6*, S. Das, J. Boatwright, and C. H. Scholz (Editors), American Geophysical Union, Washington, D.C., **37**, 269–274.
- Kamae, K., and K. Irikura (1992). Prediction of site-specific strong ground motion using semiempirical methods, in *Earthquake Engineering, Tenth World Conference, 1992*, Madrid, Spain.
- Kamae, K., and K. Irikura (1998). Source model of the 1995 Hyogo-ken Nanbu earthquake and simulation of near-source ground motion, *Bull. Seism. Soc. Am.* **88**, 400–412.
- Kamae, K., K. Irikura, and A. Pitarka (1998). A technique for simulating strong ground motion using Hybrid Green's function, *Bull. Seism. Soc. Am.* **88**, 357–367.
- Liu, H. L., and D. V. Helmberger (1985). The 23:19 aftershock of the 15 October 1979 Imperial valley earthquake: more evidence for an asperity, *Bull. Seism. Soc. Am.* **75**, 689–708.
- Olsen, K. B., and R. J. Archuleta (1996). Three-dimensional simulation of earthquakes on the Los Angeles faults system, *Bull. Seism. Soc. Am.* **86**, 575–596.
- Pitarka, A. (1999). 3D elastic finite-difference modelling of seismic motion using staggered-grid with non-uniform spacing, *Bull. Seism. Soc. Am.* **89**, 54–68.
- Pitarka, A., K. Irikura, T. Iwata, and H. Sekiguchi (1998). Three-dimensional simulation of the near-fault ground motion for the 1995 Hyogoken Nanbu (Kobe), Japan, earthquake, *Bull. Seism. Soc. Am.* **88**, 428–440.
- Saikia, C. K. (1994). Modified frequency-wavenumber algorithm for regional seismograms using Filon's quadrature: modelling of L_g waves in eastern North America, *Geophys. J. Int.* **118**, 142–158.
- Sekiguchi, H., K. Irikura, T. Iwata, Y. Takehi, and M. Hoshihara (1996). Minute locating of fault planes and source process of the 1995 Hyogoken-Nanbu earthquake from the waveform inversion of strong motion, *J. Phys. Earth* **44**, 473–487.
- Silva, W. J., I. G. Wong, and R. B. Darragh (1995). Engineering characterization of earthquake strong ground motions in the Pacific Northwest, in *Assessing Earthquake Hazards and Reducing Risk in the Pacific Northwest, U.S. Geol. Surv. Profess. Pap. 1560*.
- Somerville, P. G. (1993). Engineering applications of strong ground motion simulation, *Tectonophysics* **218**, 195–219.
- Somerville, P. G., M. Sen, and B. Cohee (1991). Simulation of strong ground motion recorded during the 1985 Michoacan Mexico and Valparaiso, Chile earthquakes, *Bull. Seism. Soc. Am.* **81**, 1–28.
- Somerville, P. G., C. Saikia, D. Wald, and R. Graves (1996). Implications of the Northridge earthquake for strong ground motions from thrust faults, *Bull. Seism. Soc. Am.* **86**, S115–S125.
- Steidl, J. H., R. Archuleta, and S. H. Hartzell (1991). Rupture of the 1989 Loma Prieta, California, earthquake, *Bull. Seism. Soc. Am.* **81**, 1573–1602.
- Vidale, J. H. (1989). Influence of focal mechanism on peak accelerations of strong motions of Whittier Narrows, California, earthquake and an aftershock, *J. Geophys. Res.* **94**, 9607–9613.
- Wald, D. J. (1996). Slip history of the 1995 Kobe, Japan earthquake determined from strong motion, teleseismic and geodetic data, *J. Phys. Earth* **44**, 489–503.
- Wald, D. J., L. J. Burdick, and P. G. Somerville (1988). Simulation of acceleration time histories close to large earthquakes, in *Earthquake Engineering and Soil Dynamics II—Recent Advances in Ground Motion Evaluation, Geotechnical Special Publication 20*, J. Lawrence Von Thunn, (Editor), American Society of Civil Engineering, New York, 430–444.
- Wald, D. J., D. V. Helmberger, and T. H. Heaton (1991). Rupture model of the 1989 Loma Prieta earthquake from the inversion of the strong-motion and broad-band teleseismic data, *Bull. Seism. Soc. Am.* **81**, 1540–1572.
- URS Greiner Woodward Clyde
566 El Dorado Street, Suite 100
Pasadena, California 91101
(A. P., P. S.)
- Izumi Research Institute
Shimizu Corporation
Fukoku Seimei Building
2-2-2 Uchisaiwai-cho, Chyoda-ku, Tokyo, 100-0011
Japan
(Y. F.)
- Power Engineering R&D Center,
Tokyo Electric Power Company
4-1, Egasaki-cho, Tsurumi-ku, Yokohama, 230-8510
Japan
(T. U.)
- Disaster Prevention Research Institute
Kyoto University
Gokasho, Uji, 611
Japan
(K. I.)

Manuscript received 29 July 1999.